

First-Principles Insights into the Role of Coordination Polyhedron Size on Mn Ion Migration within $\text{Li}_{2-x}\text{MnO}_3$ Layered Cathode Material

Huiying Zhang, Dongsen Wu, Fanghua Ning,* Yiming Guo, Jingwen Dai, Zhusuo Sun, Xiaoyu Liu, Shigang Lu, and Jin Yi*

Li-rich cathode materials are promising cathode materials for lithium-ion batteries. However, the Mn ion migration in Li-rich cathode materials during charge-discharge cycles significantly impedes their practical application. In this study, a systematical investigation has been carried out to reveal the Mn ion migration mechanisms in $\text{Li}_{2-x}\text{MnO}_3$ by using first-principles calculations. It is found that the Mn migration energy increases with increasing Li^+ extraction from Li_2MnO_3 . Conversely, the Li_{Mn} anti-site formation energy declines with the extraction of more Li^+ from Li_2MnO_3 . The migration energy decreases under

the tensile strain along the c- and b-axes. Further investigations reveal that the Mn ion migration energy is determined by MnO_6 coordination polyhedron. Specifically, a larger MnO_6 coordination polyhedron volume would result in lower migration energy, highlighting the coordination polyhedron size as a pivotal factor in the suppression of Mn ion migration. This study offers an in-depth understanding of transition metal ion migration phenomena, providing theoretical guidance for devising strategies to mitigate Mn migration in Li-rich materials.

1. Introduction

Layered lithium transition metal oxides, such as LiTMO_2 ($\text{TM} = \text{Ni}, \text{Co}, \text{Mn}$), have been widely used as cathode materials for rechargeable lithium-ion batteries (LIBs).^[1] In recent years, Li-rich layered cathode materials $x\text{Li}_2\text{MnO}_3 \cdot (1-x)\text{LiTMO}_2$, have attracted significant attention due to their ultrahigh energy density ($> 250 \text{ mAh g}^{-1}$).^[2] Li_2MnO_3 , also known as $\text{Li}[\text{Li}_{1/3}\text{Mn}_{2/3}]_{\text{O}}_2$, exhibits an oxygen stacking pattern similar to LiTMO_2 , while one-third of the transition metal in the transition metal layer is replaced by lithium. Li_2MnO_3 serves as a source of excess lithium ions and plays a dominant role in achieving high capacity, whose theoretical capacity is 458 mAh g^{-1} .^[3] Understanding the structural characteristics of the pure-phase Li_2MnO_3 is of significant importance for elucidating structural transformations and electrochemical properties in layered lithium-rich materials.

The phase transformation from layered to spinel phase in lithium-rich cathode materials is a critical factor leading to voltage fade and voltage hysteresis,^[4] which is mainly induced by Mn migration.^[5] The Mn ion migration from the transition layer to the Li layer would result in irreversible structural degradation.^[6] Thus, structural modification strategies, such as elemental substitution and surface coating, have been proposed to inhibit Mn ion migration and stabilize the framework.^[7] It is found that substituting

Mn with Sn or Ru in Li-rich Mn-based cathode material would suppress Mn ion migration, owing to the larger ionic size of Sn and Ru ions.^[8] Controlling the coordination environment of oxygen can inhibit irreversible structural transformation.^[9] For example, it is reported that Mn ion migration and voltage fade can be suppressed by preparing lithium-rich layered materials with surface layered/spinel heterostructures and lithium deficiencies.^[10] Graphene coating has been proposed as a strategy to inhibit Mn ion migration, confirmed by experiments and first-principles calculations.^[11] Theoretical research on the molecular orbitals of manganese-based lithium-rich configurations has offered guidance for the development of high-performance batteries.^[12] Persson et al. elucidated the migration of Mn ions in $\text{Li}_{2-x}\text{MnO}_3$ ($0 \leq x \leq 2$) as a function of Li content by using first-principles calculations.^[5b] It is found that Mn ion migration becomes thermodynamically favorable when the lithium content is below a certain threshold ($x > 1$). Moreover, Islam et al. found that oxygen dimerization in $\text{Li}_{2-x}\text{MnO}_3$ would promote the migration of Mn ions onto octahedral sites of Li layers.^[13] However, the intrinsic mechanisms accounting for the enhanced structural stability remain elusive.

In this work, first-principles calculations were used to gain a deeper insight into the migration mechanism of Mn. It is found that the Mn migration energy increases with increasing Li^+ extraction from Li_2MnO_3 . The impact of uniaxial strain on Mn ion migration within $\text{Li}_{2-x}\text{MnO}_3$ has been explored. The changes in lattice parameters, interlayer distances, MO_6 spatial size, migration energy, and migration pathways demonstrate that the coordination polyhedron size is the key factor that affects Mn ion migration in $\text{Li}_{2-x}\text{MnO}_3$. Specifically, a larger MnO_6 coordination polyhedron volume would result in lower migration energy. Furthermore, Li_{Mn} anti-site formation energy in $\text{Li}_{2-x}\text{MnO}_3$ further

H. Zhang, D. Wu, F. Ning, Y. Guo, J. Dai, Z. Sun, X. Liu, S. Lu, J. Yi
Institute for Sustainable Energy/College of Sciences

Shanghai University

Shanghai 200444, China

E-mail: fhning@shu.edu.cn

jin.yi@shu.edu.cn

 Supporting information for this article is available on the WWW under <https://doi.org/10.1002/batt.202500044>

elucidates the correspondence between spatial size and anti-site formation energy. A comprehensive understanding of the Mn ion migration mechanisms is essential for providing theoretical guidance in engineering Li-rich cathode materials.

2. Results and Discussion

2.1. The Delithiated States of Li_2MnO_3

Li_2MnO_3 ($\text{Li}[\text{Li}_{1/3}\text{Mn}_{2/3}]\text{O}_2$) is a layered material characterized by the $\text{C}2/\text{m}$ space group, which features an oxygen stacking pattern that is analogous to the arrangement found in LiTMO_2 ($\text{TM} = \text{Co, Ni, Mn}$). The Li sites within Li_2MnO_3 are categorized into 2c and 4h sites within the Li layers, and 2b sites within the TM layers, as delineated in Figure 1a. Each Li^+ is surrounded by six neighboring transition metal atoms within TM layers, forming a "honeycomb" superstructure. The structural evolution of Li_2MnO_3 during delithiation is revealed by using first-principles calculations. The delithiation sites would significantly affect the thermodynamic stability of the $\text{Li}_{2-x}\text{MnO}_3$. For instance, Koyama et al. reported three configurations for $\text{Li}_{1.5}\text{MnO}_3$, among which the model with vacancies at 4h sites exhibited the lowest energy compared to the models with vacancies at 2c or 2b sites.^[14] It is crucial to determine the delithiated state models.^[15] We constructed different delithiation models with varying Li-vacancy patterns (Table S1, Supporting Information). The delithiated configuration with the lowest total energy aligns with the stable configurations reported by Persson et al.^[16] The optimal delithiation models of $\text{Li}_{2-x}\text{MnO}_3$ ($x = 0.00, 0.50, 0.75, 1.00, 1.50, 2.00$) have been achieved. Figure 1b illustrates the volume and lattice parameter variation upon delithiation. The optimal delithiation models of $\text{Li}_{2-x}\text{MnO}_3$ are shown in Figure 1c-f. The final delithiation model

of $\text{Li}_{2-x}\text{MnO}_3$, as elucidated in Table S2, Supporting Information, presents five ground states with varying Li concentrations at 2c , 4h , and 2b sites. In the process of lithium extraction from Li_2MnO_3 , initially, half of the lithium ions are removed from the 4h site, resulting in the formation of $\text{Li}_{1.50}\text{MnO}_3$. This is followed by the subsequent removal of the remaining lithium ions from the 2b site, leading to the complete depletion of lithium ions at the 2b site in Li_1MnO_3 . Figure S1, Supporting Information, shows the projected density of states (PDOS) of $\text{Li}_{2-x}\text{MnO}_3$ ($x = 0.00, 0.50, 0.75$, and 1.00). In the pristine Li_2MnO_3 ground state, Mn^{4+} exhibits the $t_{2g}^3 e_g^0$ electronic configuration, oxygen-dominated charge compensation occurs via progressive O- $2p$ hole formation at the valence band during delithiation, while Mn- $3d$ electronic configurations remain nearly unchanged. The volume and lattice parameters of layered $\text{Li}_{2-x}\text{MnO}_3$ show significant changes with the variation of lithium concentration. Enhanced delithiation induces a progressive volume reduction in $\text{Li}_{2-x}\text{MnO}_3$, particularly accentuated at lower lithium contents ($x = 0.5$), where a distinct structural phase transition leads to a sharp volume decrease. Particularly, in the delithiation state $\text{Li}_{0.5}\text{MnO}_3$, a notable phase transition is observed, characterized by TM layer gliding from the $\text{O}3$ to $\text{O}1$ stacking sequence. This finding aligns with the results obtained from previous first-principles computational studies.^[17]

As x in $\text{Li}_{2-x}\text{MnO}_3$ increases within the range of $0.5 \leq x \leq 1$, the $\text{Li}_{2-x}\text{MnO}_3$ remains $\text{O}3$ stacking sequence. This study focuses on the delithiated states of $\text{Li}_{2-x}\text{MnO}_3$ with $0.5 \leq x \leq 1$. The lattice parameter a is almost unchanged. In contrast, the lattice parameter c exhibits a monotonic increase, while parameter b undergoes a corresponding decrease. The lithium extraction from the TM layers for $0.5 \leq x \leq 1$ is responsible for the decrease of the lattice parameter b . As shown in Figure S2, Supporting Information, the contraction of Mn-O bond lengths during

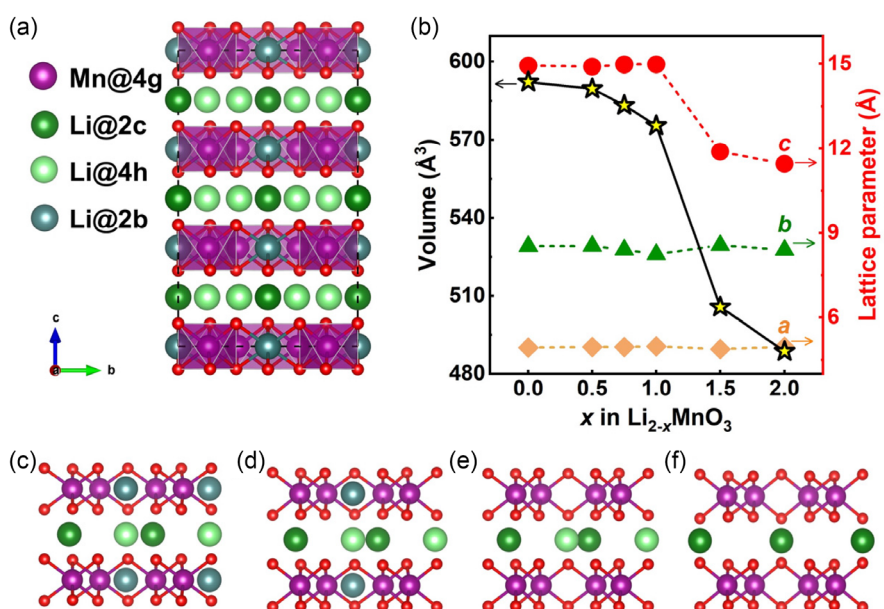


Figure 1. a) Crystal structure of Li_2MnO_3 . b) The evolution of lattice parameters and volume during delithiation. The Li/vacancy configurations for the $\text{Li}_{2-x}\text{MnO}_3$ of c) $x = 0.50$, d) $x = 0.75$, e) $x = 1.00$, and f) $x = 1.50$.

lithium extraction is more pronounced in the range of $0.5 \leq x \leq 1.0$ than in the range of $0.0 \leq x \leq 0.5$, consistent with the variation trend of lattice parameter b . These observations demonstrate that Li removal from the TM layer reduces TM—O bond lengths, thereby shrinking the lattice parameter b .

To investigate the reasons for the increased trends in lattice parameter c , both tensile and compressive strains were conducted along the c -axis to further compare the variation in interlayer spacing. Further analysis into the bond length changes and the coordination polyhedron size during delithiation was conducted. The volume change rate listed in Table S3, Supporting Information, reflects the average strain across the three-dimensional lattice parameters. Based on the volume change rate of $\text{Li}_{2-x}\text{MnO}_3$ during delithiation process with $0.0 \leq x \leq 1.0$, a strain range of $\pm 4\%$ was chosen. It is generally believed that the removal of a significant amount of lithium results in a substantial reduction in LiO_6 interlayer spacing in layered structures.^[18] As shown in Figure 2a, as x in $\text{Li}_{2-x}\text{MnO}_3$ ($0.5 \leq x \leq 1$) rises, the Li—O interlayer spacing decreases monotonically, whereas the Mn—O interlayer spacing exhibits an increase. Furthermore, simulations involving both tensile and compressive strains along the c -axis have been carried out. Changes in Li—O interlayer spacing under strains along the c -axis are more pronounced than those of Mn—O interlayer spacing, suggesting that strain is mainly absorbed by the Li—O layers. Li—O interlayer spacing decreases while Mn—O interlayer spacing increases during delithiation processes. Consequently, the difference between Mn—O and Li—O interlayer spacing is reduced. The

variation trend of lattice parameter c during delithiation is predominantly determined by the Mn—O interlayer spacing. With increasing Li^+ extraction from Li_2MnO_3 , the average bond lengths of Li—O and Mn—O monotonically decrease (Figure 2b). Specifically, although the average bond length of Li—O and Mn—O decreases monotonically with increasing Li^+ extraction, the projection of the Mn—O bond length along the c -axis increases, thus the Mn—O interlayer spacing increases, suggesting that the expansion trend of the Mn—O interlayer spacing is correlated with the orientation of the Mn—O bonds.

To investigate the variation in the orientation of the Mn—O bonds, the local structure of the MnO_6 octahedron has been analyzed. As shown in Figure 2c, the increased extent of lithium extraction promotes the formation of O—O dimers within the MnO_6 octahedron, the detailed O—O distances are listed in Table S4, Supporting Information. The formation of O—O dimers would result in an increasing dihedral angle between the MnO_2 —Mn plane and the (010) plane (Figure 2d), which influences the orientation of the Mn—O bonds. $\text{Li}_{2-x}\text{MnO}_3$ exhibits contraction of the Li—O layers alongside the expansion of Mn—O layers, whereas LiCoO_2 shows expansion of Li—O layers and contraction of the Co—O layer. A key structural distinction lies in the TM layers. Specifically, Li_2MnO_3 contains Li within its TM layers, while LiCoO_2 does not. In LiCoO_2 , the TM layers function as an integrated unit during delithiation or when subjected to strain. The charge distribution around Co atoms adjusts dynamically with changes in Li content, leading to continuous charge redistribution between Co and O during delithiation.

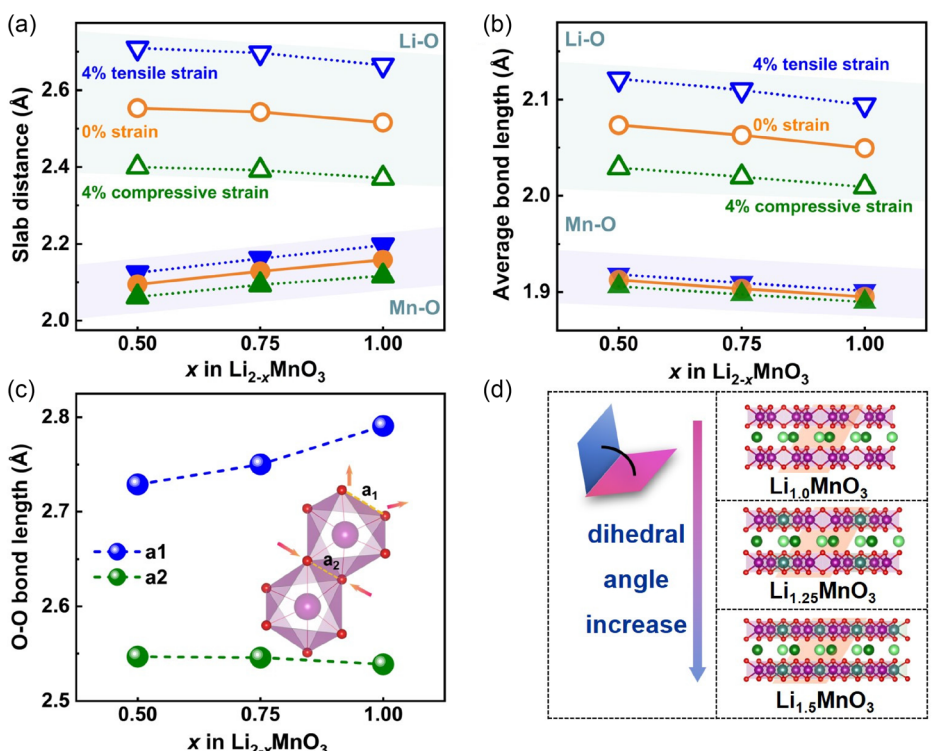


Figure 2. a) The layer spacing of Li and LiMn_2 slab layers in $\text{Li}_{2-x}\text{MnO}_3$ ($0.5 \leq x \leq 1$). b) The average bond length of the Li—O bond within the Li slab and Mn—O bond in $\text{Li}_{2-x}\text{MnO}_3$ ($0.5 \leq x \leq 1$). c) The O—O distances variation upon delithiation. d) The schematic of the dihedral angle between the MnO_2 —Mn plane and the (010) plane in $\text{Li}_{1.0}\text{MnO}_3$, $\text{Li}_{1.25}\text{MnO}_3$, and $\text{Li}_{1.5}\text{MnO}_3$.

In contrast, in Li_2MnO_3 , the highly oxidized Mn^{4+} is resistant to further oxidation. Therefore, charge compensation mainly depends on the oxidation of oxygen ions, which induces O–O dimerization. It is found that O–O dimerization is responsible for the distinct trends of layer spacing changes during delithiation observed in Li_2MnO_3 and LiCoO_2 .

2.2. Mn Ion Migration during Delithiation

Then, Mn ion migration is systematically investigated. The transition of Li_2MnO_3 from a layered to a spinel structure is commonly characterized by the migration of Mn ions from the TM layers to the nearest Li vacancies in the Li layers, as described in Figure 3a. Both Li and TM occupy octahedral positions in a face-centered cubic lattice. Two migration pathways for Mn ion migration in $\text{Li}_{1.5}\text{MnO}_3$ have been considered, as depicted in Figure 3b. The first path is that the Mn ion directly migrates across a facet to the nearest octahedral site within the Li layer. The second path is that the Mn ion migrates via tetrahedral sites between two adjacent octahedral sites. The migration barrier of the second pathway is lower, indicating that the tetrahedral site is the optimal site for Mn ion at the transition state. It is worth noting that the first-principles calculations face inherent constraints from limited supercell sizes. The $\text{Li}_{2-x}\text{MnO}_3$ models in this work contain 12 Mn atoms, corresponding to a Mn migration defect concentration of 8.3% (1/12), which is much higher than that of experimental conditions during realistic charging. Thus, the migration energy barriers obtained from first-principles calculations should be interpreted in terms of relative values in the same conditions.

During delithiation, variations occur in the lattice parameters and the volume of layered $\text{Li}_{2-x}\text{MnO}_3$, and Mn ion migration would be tuned. Figure 3c illustrates the Mn migration energy within TM layers and from TM layers to octahedral Li-layer sites in $\text{Li}_{2-x}\text{MnO}_3$ ($0.5 \leq x \leq 1$). In-plane Mn migration within TM layers requires lower activation energy compared to interlayer migration, as it preserves the overall layered framework while perturbing the honeycomb superlattice ordering within the TM layers. At $x = 0.5$, due to the absence of lithium vacancies in the TM layer, the system does not undergo in-plane Mn migration. When Mn ion migrates from the octahedral site within the transition metal layer to the lithium layer, the Mn migration energy increases as more Li^+ is extracted from Li_2MnO_3 . The spacing between the transition metal layers expands, while the spacing between the lithium layers that manganese migrates to contracts, as shown in Figure 3d. The spacing between other transition metal layers and lithium layers, where ion migration does not occur, remains predominantly unchanged. The migration of Mn ions from the TM layer into the Li layer reduces the Li–O interlayer spacing. However, the Mn–O interlayer spacing is increased. Oxygen dimerization plays a crucial role in promoting the structural transition of $\text{Li}_{2-x}\text{MnO}_3$ and significantly impacts Mn migration. O–O distance is highly influenced by the electron density of oxygen atoms. This electron density fluctuates in accordance with the degree of delithiation in $\text{Li}_{2-x}\text{MnO}_3$. With the increase x in $\text{Li}_{2-x}\text{MnO}_3$, O–O distance is shortened, facilitating O–O dimerization at deep delithiated states.^[19] The two-dimensional differential charge density maps projected along the Mn–O₂–Mn planes for $\text{Li}_{1.5}\text{MnO}_3$ and the O1-phase MnO_3 are shown in Figure S3, Supporting Information. The comparative analysis indicates that

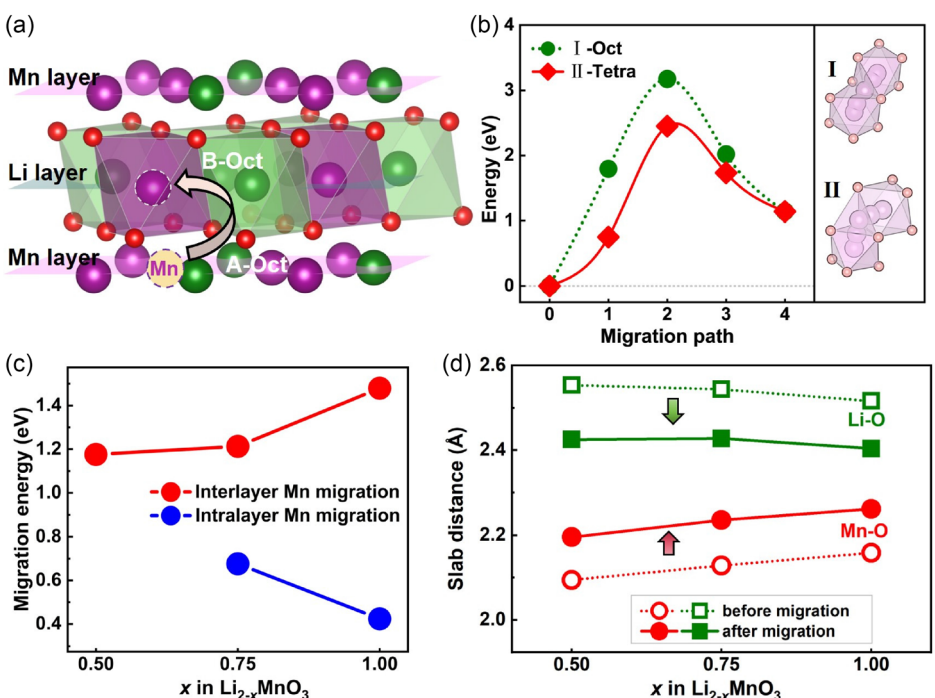


Figure 3. a) The schematic of Mn migration from the Mn layer to the Li layer within $\text{Li}_{2-x}\text{MnO}_3$. b) Two paths and the corresponding energy profiles for Mn migration in $\text{Li}_{1.5}\text{MnO}_3$. c) The migration energy of Mn within the TM layer and from the TM layer to the octahedral position of the Li layer in $\text{Li}_{2-x}\text{MnO}_3$. d) The layer spacing of Li and LiMn_2 slab layers before and after Mn migration in $\text{Li}_{2-x}\text{MnO}_3$.

the fully delithiated MnO_3 system, characterized by a smaller O–O dimer distance, exhibits enhanced O–O covalent interactions, which is evidenced by intensified electron accumulation between adjacent oxygen atoms. Simultaneously, the Mn–O bonding strength is weakened compared to that in $\text{Li}_{1.5}\text{MnO}_3$. These findings suggest that O–O dimerization destabilizes the Mn–O coordination interaction, thereby potentially facilitating Mn ion migration. Given the crucial role of O–O dimerization in Mn ion migration, designing the lithium interlayer spacing for the purpose of inhibiting Mn migration in Li-rich layered cathode materials might present greater challenges in comparison to traditional layer cathode materials (LiTMO_2).

2.3. The Key Factor that Affects Mn Ion Migration

To reveal the key factor that affects Mn ion migration, Mn ion migration energies under tensile and compressive strain have been calculated (Figure 4a). The tensile strain along the c-axis leads to a decrease in Mn ion migration energy, while compressive strain has the opposite effect. Thus, the spatial size of the local structure plays a crucial role in Mn ion migration. Figure S4, Supporting Information, shows the MnO_6 coordination polyhedra before and after Mn ion migration. The correlation between the migration energy and the size of the MnO_6 coordination polyhedron size before Mn migration has been analyzed (Figure 4b). When the volume of the MnO_6 octahedron decreases,

the migration energy increases. The Mn ion migration energy increases with increasing Li^+ extraction from Li_2MnO_3 , as mentioned earlier. As more lithium is extracted from Li_2MnO_3 , the MnO_6 coordination polyhedra show a smaller size, thereby leading to a higher migration energy.

The migration of Mn from the TM layer to the octahedral sites within the Li layer instigates structural adjustments within the crystal lattice. Due to the distinct ionic sizes and net charges between Mn and Li ions, the occupation of Mn ions at Li sites would lead to a decrease in Li–O interlayer spacing. Particularly, the extraction of Li^+ , as well as Mn ion migration would promote O–O dimerization. O–O dimerization profoundly influences the lattice parameters and Mn–O interlayer spacing. To further elucidate the correspondence between Mn ion migration energy and the spatial configuration of $\text{Li}_{2-x}\text{MnO}_3$, strains along the b-axis have been applied. As shown in Figure 4c, compression strain leads to a reduction in the volume of the MnO_6 coordination octahedron in $\text{Li}_{1.25}\text{MnO}_3$, thereby increasing the migration energy for Mn to move to the Li layer. The migration energy $\text{Li}_{1.25}\text{MnO}_3$ shows the same variation trend under strains along the c- and b-axes. Notably, the migration energy changes under strain along the b-axis are more significant compared to those observed under strain along the c-axis. Changes in the Mn–O bond length within the MnO_6 octahedron for the migrating Mn ion before and after migration in $\text{Li}_{1.25}\text{MnO}_3$ under strain along the c-axis and b-axis are shown in Figure S5, S6, Supporting Information, respectively. The volume change of

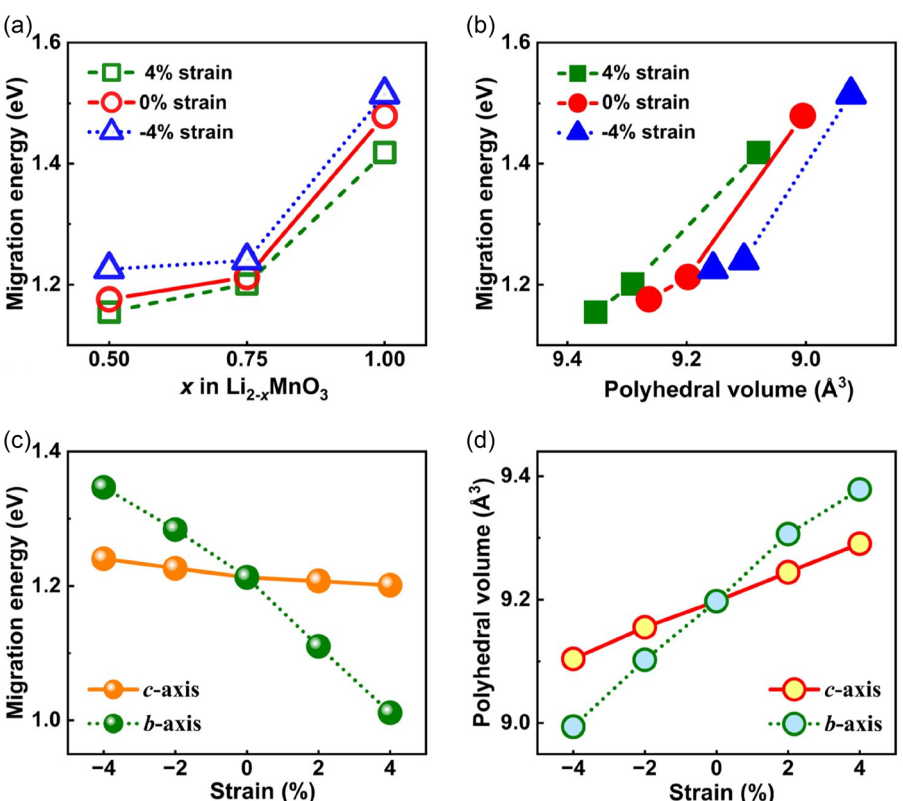


Figure 4. a) The migration energy for Mn migrates to octahedral sites within the Li layer in $\text{Li}_{2-x}\text{MnO}_3$ under strain along the c-axis. b) The relationship between the migration energy and size of MnO_6 coordination polyhedra under strain along the c-axis. The comparative variation in migration energy and c) the volume of MnO_6 coordination polyhedra d) in $\text{Li}_{1.25}\text{MnO}_3$ under uniaxial strain along the c- and b-axis.

MnO_6 coordination polyhedra under strain along the b-axis is more significant than that under strain along the c-axis (Figure 4d). Therefore, the migration energy is more sensitive to the change in strain along the b-axis than to the change in strain along the c-axis. The migration energy for Mn ion migration to the octahedral sites within the Li layer exhibits a consistent correlation with the variations in the spatial size of the MnO_6 coordination polyhedron before migration. Thus, the coordination polyhedron size is the key factor of the Mn ion migration energy.

To further demonstrate the crucial role of the coordination polyhedron size, we additionally calculated the formation energy of Li_{Mn} anti-site defect in $\text{Li}_{2-x}\text{MnO}_3$ ($0 \leq x \leq 1$). The Li_{Mn} anti-site energy decreases with increasing Li^+ extraction from Li_2MnO_3 without strain (Figure 5). The variation trends in Mn migration energy and anti-site formation energy as a function of x in $\text{Li}_{2-x}\text{MnO}_3$ exhibit different behavior. As more Li^+ is extracted from Li_2MnO_3 , the vacancies in the Li layer increase, and coordination polyhedron size decreases. To control the variables, we analyzed the impact of polyhedral size changes on Mn ion migration energy while keeping the Li content constant. In the four different delithiation stages of $\text{Li}_{2-x}\text{MnO}_3$ ($x = 0.00, 0.50, 0.75$, and 1.00), the correlation between the formation energy of Li_{Mn} anti-site and MnO_6 polyhedral volume under strain along the c- and b-axis is shown in Figure S7, Supporting Information. The Li_{Mn} anti-site formation energy under strain does not exhibit a monotonic

variation in $\text{Li}_{2-x}\text{MnO}_3$. Instead, at each delithiation stage, the Li_{Mn} anti-site formation energy exhibits a "U-shaped" curve as a function of octahedral volume, indicating that there is an optimal volume that minimizes the formation energy of the defects, and optimal volume decreases progressively as delithiation stage increases. The factors that affect the Li_{Mn} anti-site formation energy are more complex than that of Mn migration energy, primarily due to the involvement of Li site transition in the anti-site configuration. The main difference between the Li_{Mn} anti-site formation and Mn ion migration is that Li_{Mn} anti-site formation involves Li^+ occupying Mn sites within the Mn–O layer. Li^+ occupying Mn sites within the Mn–O layer would need a larger volume of coordination octahedron, which become the main factor affecting Li_{Mn} anti-site formation energy. Thus, the trend of Li_{Mn} anti-site formation energy is attributed to the coupling between the sizes of MnO_6 and LiO_6 octahedra.

Combining the variation in Mn ion migration energy and Li_{Mn} anti-site formation energy as a function of the volume of MnO_6 coordination octahedron, the crucial role of the MnO_6 coordination octahedral size on the structural stability of $\text{Li}_{2-x}\text{MnO}_3$ is highlighted, which is essential to the electrochemical performance of Li-rich cathode material. The coordination polyhedra size has a profound influence on the interlayer migration of Mn ions. Thus, it is demonstrated that the size of the MO_6 coordination polyhedra is crucial in determining the structural stability of Li-rich cathode materials.

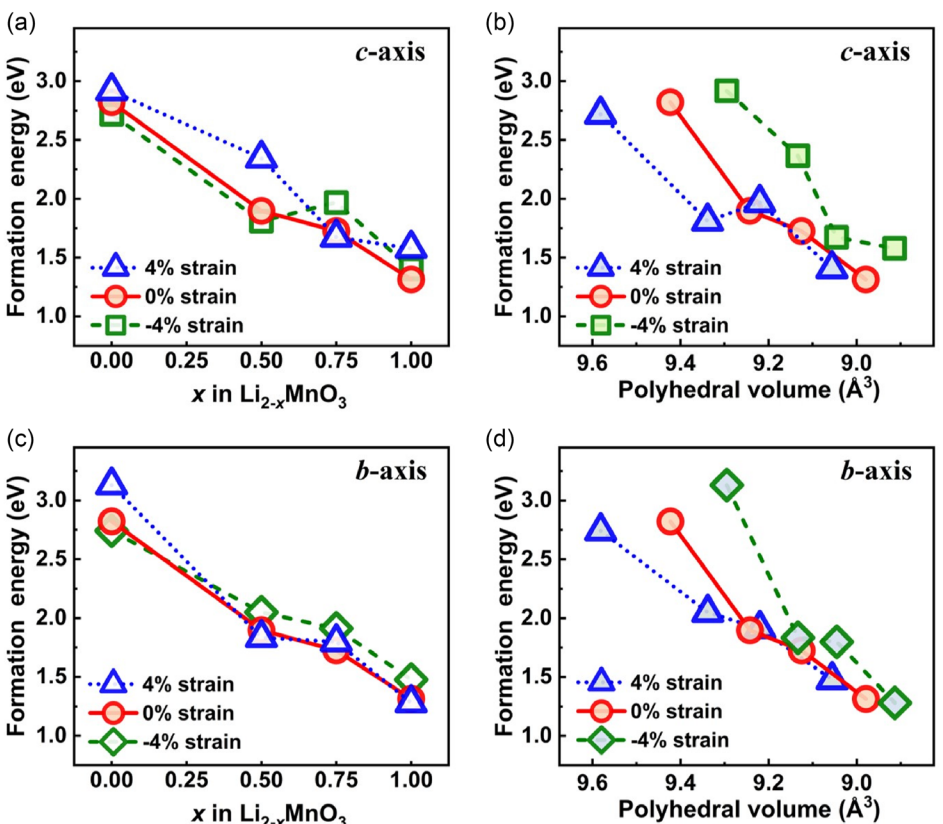


Figure 5. a) The formation energies of Li_{Mn} anti-site in $\text{Li}_{2-x}\text{MnO}_3$ and b) the correlation between the formation energies and the size of MnO_6 coordination polyhedra under strain along the c-axis. c) The formation energies of Li_{Mn} anti-site in $\text{Li}_{2-x}\text{MnO}_3$ and d) the correlation between the formation energies and the size of MnO_6 coordination polyhedra under strain along the b-axis.

3. Conclusion

In summary, a comprehensive investigation has been conducted to investigate the factors that affect Mn ion migration in $\text{Li}_{2-x}\text{MnO}_3$ by using first-principles computational methods. The transition from the O3 to the O1 phase is observed in $\text{Li}_{0.5}\text{MnO}_3$. The variations in lattice parameters and layer spacing during lithium extraction of Li_2MnO_3 are provided. The average bond length of Li–O and Mn–O decreases monotonically with increasing Li^+ extraction, whereas the projection of the Mn–O bond length along the c-axis increases due to the change in orientation of the Mn–O bonds, thus the Mn–O interlayer spacing increases. The Mn migration energy increases as more Li^+ is extracted from Li_2MnO_3 . Moreover, the migration energy variations under uniaxial strain along the c- and b-axes have been calculated. The migration energy decreases under the tensile strain along the c- and b-axes. Further investigations revealed the intricate relationship between the migration energy and the size of the MnO_6 coordination polyhedron. It is found that the spatial size is the key factor in suppressing Mn ion migration. Larger MnO_6 coordination polyhedron volume would result in lower migration energy. A comprehensive understanding of the Mn ion migration mechanisms is essential for providing vital theoretical guidance in the development of Li-rich cathode materials. The calculation results of Li_{Mn} anti-site formation energy in $\text{Li}_{2-x}\text{MnO}_3$ further elucidate the correspondence between spatial size and anti-site formation energy. This work highlights the significant influence of the size of the MnO_6 coordination polyhedron on Mn ion migration, offering valuable theoretical insights to enhance the structural stability of Li-rich cathode materials.

4. Methodology

First-principles calculations are conducted using DS-PAW software with the projector-augmented wave (PAW) method, a density functional theory (DFT)-based platform.^[20] A plane-wave basis set with an energy cutoff of 520 eV is employed. The Brillouin zone is sampled using a $5 \times 3 \times 2$ k-point mesh according to the Monkhorst–Pack scheme.^[21] The exchange functional is approximated by the Perdew–Burke–Ernzerhof (PBE) formulation, a variant within the family of generalized gradient approximation (GGA).^[22] The Hubbard U correction (GGA + U) accounts for the strong correlation effect in transition metals,^[23] with a U value of 4.5 eV for the 3d state of Mn, derived from previous theoretical studies.^[5b,24] The energy convergence of self-consistent iteration is determined by an energy difference of less than 10^{-5} eV. The force for each atom in atomic position optimization is less than $0.01 \text{ eV } \text{\AA}^{-1}$. The migration pathway and energy barrier of the transition metal ions were determined using the Climbing Image Nudged Elastic Band (CI-NEB) method,^[25] with three intermediate configurations inserted to generate the minimum energy path (MEP). The Li_2MnO_3 structure is modeled in a $2 \times 1 \times 2$ supercell, containing 72 atoms in total. The Li_{Mn} antisite configurations were generated by atomic substitution within a fixed unit cell framework. Strain was applied by modifying the unit cell lattice parameters. The uniaxial strain (ε) is defined as

the ratio of the lattice parameter change (Δa) in the corresponding direction to the original lattice constant (a) (i.e., $\varepsilon = \Delta a/a$).

Acknowledgements

This work was supported by the National Natural Science Foundation of China (grant nos. 52402286, 22075171, and 22379090), and the Shanghai Sailing Program (grant no. 24YF2712300). The authors gratefully acknowledge HZWTECH for providing computation facilities.

Conflict of Interest

The authors declare no conflict of interest.

Data Availability Statement

The data that support the findings of this study are available from the corresponding author upon reasonable request.

Keywords: first-principles calculations • lithium-ion batteries • lithium-rich cathode materials • Mn ion migration

- [1] a) M. Li, J. Lu, Z. Chen, K. Amine, *Adv. Mater.* **2018**, *30*, 1800561; b) B. Li, J.-M. Tarascon, *Comprehensive Inorganic Chemistry III*, Vol. 7 (Eds: J. Reedijk, K. R. Poeppelmeier), Elsevier, Amsterdam **2023**.
- [2] D.-H. Seo, J. Lee, A. Urban, R. Malik, S. Kang, G. Ceder, *Nat. Chem.* **2016**, *8*, 692.
- [3] R. Shunmugasundaram, R. S. Arumugam, J. R. Dahn, *J. Electrochem. Soc.* **2016**, *163*, A1394.
- [4] a) D. Eum, B. Kim, S. J. Kim, H. Park, J. Wu, S.-P. Cho, G. Yoon, M. H. Lee, S.-K. Jung, W. Yang, W. M. Seong, K. Ku, O. Tamwattana, S. K. Park, I. Hwang, K. Kang, *Nat. Mater.* **2020**, *19*, 419; b) J.-J. Marie, R. A. House, G. J. Rees, A. W. Robertson, M. Jenkins, J. Chen, S. Agrestini, M. Garcia-Fernandez, K.-J. Zhou, P. G. Bruce, *Nat. Mater.* **2024**, *23*, 818; c) L. He, Z. Gu, Y. Zhang, H. Jing, P. Li, *Energy Fuels* **2023**, *37*, 4835.
- [5] a) Y. Gao, J. Ma, Z. Wang, G. Lu, L. Chen, *Phys. Chem. Chem. Physics* **2017**, *19*, 7025; b) E. Lee, K. A. Persson, *Adv. Energy Mater.* **2014**, *4*, 1400498.
- [6] a) W. Huang, L. Yang, Z. Chen, T. Liu, G. Ren, P. Shan, B. W. Zhang, S. Chen, S. Li, J. Li, C. Lin, W. Zhao, J. Qiu, J. Fang, M. Zhang, C. Dong, F. Li, Y. Yang, C. J. Sun, Y. Ren, Q. Huang, G. Hou, S. X. Dou, J. Lu, K. Amine, F. Pan, *Adv. Mater.* **2022**, *34*, 2202745; b) T. Lin, T. Seaby, Y. Hu, S. Ding, Y. Liu, B. Luo, L. Wang, *Electrochem. Energy Rev.* **2022**, *5*, 27.
- [7] a) M. Y. Yang, S. Kim, K. Kim, W. Cho, J. W. Choi, Y. S. Nam, *Adv. Funct. Mater.* **2017**, *27*, 1700982; b) P. Huang, X. Ding, J. Cui, H. Xie, C. Liu, D. Luo, *Energy Fuels* **2023**, *37*, 4682; c) T. Zeng, M. Yang, F. Sun, Z. Huang, W. Zhao, Z. Chen, D. Zou, J. Qiu, L. Wang, R. Wang, C. Zhang, T. Yang, W. Ji, J. Xu, W. Yin, R. Li, H. Meng, Y. Xiao, *Adv. Funct. Mater.* **2024**, *34*, 2411542.
- [8] a) M. Sathiya, K. Ramesha, G. Rousse, D. Foix, D. Gonbeau, A. S. Prakash, M. L. Doublet, K. Hemalatha, J. M. Tarascon, *Chem. Mater.* **2013**, *25*, 1121; b) Y. Wang, Z. Yang, Y. Qian, L. Gu, H. Zhou, *Adv. Mater.* **2015**, *27*, 3915.
- [9] a) X. Liu, J. Cheng, Y. Guan, S. Huang, F. Lian, *Mater. Chem. Front.* **2023**, *7*, 3434; b) B. Wang, Z. Zhuo, H. Li, S. Liu, S. Zhao, X. Zhang, J. Liu, D. Xiao, W. Yang, H. Yu, *Adv. Mater.* **2023**, *35*, 2207904.
- [10] a) Y. Chen, G. Li, Z. Xie, P. Huang, X. Li, F. Li, W. Yan, *Energy Fuels* **2023**, *37*, 6800; b) Y. Jiang, F. Yu, W. Ke, L. Deng, Y. Xia, X. Li, L. Que, N. Zhang, L. Zhao, Z. Wang, *Adv. Funct. Mater.* **2023**, *33*, 2213615.
- [11] F. Ning, H. Shang, B. Li, N. Jiang, R. Zou, D. Xia, *Energy Storage Mater.* **2019**, *22*, 113.
- [12] H. Yang, L. Wang, Y. Li, Z. Zhuo, T. Wu, J. Liu, L. Xu, H. Du, S. Liu, L. Wu, S. Zhao, M. Tang, W. Yang, H. Yu, *Proc. Natl. Acad. Sci.* **2024**, *121*, e2412460121.
- [13] H. Chen, M. S. Islam, *Chem. Mater.* **2016**, *28*, 6656.

- [14] Y. Koyama, I. Tanaka, M. Nagao, R. Kanno, *J. Power Sources* **2009**, *189*, 798.
- [15] a) M. Ha, A. Hajibabaei, D. Y. Kim, A. N. Singh, J. Yun, C. W. Myung, K. S. Kim, *Adv. Mater.* **2022**, *12*, 2201497; b) S. Y. Willow, A. Hajibabaei, M. Ha, D. C. Yang, C. W. Myung, S. K. Min, L. Geunsik, S. K. Kwang, *Chem. Phys. Rev.* **2024**, *5*, 041307.
- [16] Y. Shin, H. Ding, K. A. Persson, *Chem. Mater.* **2016**, *28*, 2081.
- [17] X. Zhang, F. Zheng, S. Wu, Z. Zhu, *Phys. Chem. Chem. Phys.* **2021**, *23*, 4829.
- [18] K. Kang, G. Ceder, *Phys. Rev. B* **2006**, *74*, 094105.
- [19] F. Li, X. Zhang, J. Lin, J. Ma, S. Zhang, G. Yang, *J. Phys. Chem. C* **2019**, *123*, 23403.
- [20] a) J. P. Perdew, J. A. Chevary, S. H. Vosko, K. A. Jackson, M. R. Pederson, D. J. Singh, C. Fiolhais, *Phys. Rev. B* **1992**, *46*, 6671; b) G. Kresse, D. Joubert, *Phys. Rev. B* **1999**, *59*, 1758.
- [21] a) G. Kresse, J. Furthmüller, *Phys. Rev. B* **1996**, *54*, 11169; b) H. J. Monkhorst, J. D. Pack, *Phys. Rev. B* **1976**, *13*, 5188.
- [22] J. P. Perdew, K. Burke, M. Ernzerhof, *Phys. Rev. Lett.* **1996**, *77*, 3865.
- [23] V. I. Anisimov, J. Zaanen, O. K. Andersen, *Phys. Rev. B* **1991**, *44*, 943.
- [24] V. N. Kothalawala, A. A. Sasikala Devi, J. Nokelainen, M. Alatalo, B. Barbiellini, T. Hu, U. Lassi, K. Suzuki, H. Sakurai, A. Bansil, *Condens. Matter* **2022**, *7*, 54.
- [25] G. Henkelman, B. P. Uberuaga, H. Jónsson, *J. Chem. Phys.* **2000**, *113*, 9901.

Manuscript received: January 18, 2025

Revised manuscript received: March 13, 2025

Version of record online: March 17, 2025